Chemical
Science

ROYAL SOCIETY
OF CHEMISTRY

EDGE ARTICLE

View Article Online
View Journal | View Issue

Cite this: *Chem. Sci.*, 2022, **13**, 5606

All publication charges for this article have been paid for by the Royal Society of Chemistry

Received 22nd February 2022
Accepted 18th April 2022

DOI: 10.1039/d2sc01110g

rsc.li/chemical-science

Highly selective generation of singlet oxygen from dioxygen with atomically dispersed catalysts†

Wenjie Ma,‡[ac] Junjie Mao,‡[d] Chun-Ting He,‡[e] Leihou Shao,[a] Ji Liu,[a] Ming Wang,[ac] Ping Yu[ac] and Lanqun Mao*[ab]

Singlet oxygen ($^1O_2$) as an excited electronic state of O_2 plays a significant role in ubiquitous oxidative processes from enzymatic oxidative metabolism to industrial catalytic oxidation. Generally, $^1O_2$ can be produced through thermal reactions or the photosensitization process; however, highly selective generation of $^1O_2$ from O_2 without photosensitization has never been reported. Here, we find that single-atom catalysts (SACs) with atomically dispersed MN_4 sites on hollow N-doped carbon (M_1/HNC SACs, M = Fe, Co, Cu, Ni) can selectively activate O_2 into $^1O_2$ without photosensitization, of which the Fe_1/HNC SAC shows an ultrahigh single-site kinetic value of 3.30×10^{10} min^{-1} mol^{-1}, representing top-level catalytic activity among known catalysts. Theoretical calculations suggest that different charge transfer from MN_4 sites to chemisorbed O_2 leads to the spin-flip process and spin reduction of O_2 with different degrees. The superior capacity for highly selective $^1O_2$ generation enables the Fe_1/HNC SAC as an efficient non-radiative therapeutic agent for *in vivo* inhibition of tumor cell proliferation.

Introduction

Dioxygen (O_2) occupies a critical position in a great variety of oxidation reactions involved in both chemical reactions and biological processes.[1–6] In aerobic biology, O_2-related oxidation reactions are achieved by a series of evolutionary metalloenzymes such as cytochrome P450 through the interaction with O_2, resulting in the formation of reactive oxygen species (ROS) such as singlet oxygen ($^1O_2$), hydroxyl radical ($^{\bullet}OH$) and superoxide anion (O_2^{-}) or reactive metal-O_2 intermediates including metal superoxo, (hydro)peroxo, and metal-oxo species.[7–11] Among the active species, $^1O_2$ with an unoccupied π^* orbital has strong electrophilicity and unique reactivity and selectivity to serve as a synthetic reagent, attracting enormous interest from both fundamental studies and practical application fields.[12–16] To this end, increasing attention has been drawn to the development of efficient approaches to highly selective generation of $^1O_2$.[17–22]

Conventional approaches to $^1O_2$ production mainly include thermal processes using enzymatic or chemical reactions and photosensitization of O_2 with rationally designed photosensitizers.[23–26] However, the production of $^1O_2$ through these approaches is always accompanied by other ROS generation. In addition, thermal processes often require harsh conditions such as rigorous pH and particular solvents.[27,28] Despite the simplicity and controllability of the photosensitization route, it faces inherent limitations like poor selectivity of $^1O_2$, photobleaching of sensitizers, and difficulty in large-scale production.[29–31] Therefore, development of new approaches to highly selective production of $^1O_2$ is of great significance not only in the investigation of $^1O_2$-related biological and physical processes but also in the development of new materials and biological tools with $^1O_2$.

Recently, single-atom catalysts (SACs) have shown considerable potential in industrial chemical processing and photo/electrochemical energy conversion with high catalytic activity and unique selectivity due to their excellent properties like maximum atom utilization efficiency, well-defined active centers, and tunable coordination environment.[32–34] Among the developed SACs, metal-nitrogen (MN_x) sites embedded in carbon skeletons represent a significant series of SACs with excellent catalytic activity toward oxygen-related reactions including the oxygen reduction reaction and advanced oxidation processes, benefitting from precise tuning of electronic structures of active sites.[35–38] Thus, MN_x SACs provide great possibilities and opportunities in the design and fabrication of

---

[a] *Beijing National Laboratory for Molecular Sciences, Key Laboratory of Analytical Chemistry for Living Biosystems, Institute of Chemistry, The Chinese Academy of Sciences (CAS), Beijing 100190, China. E-mail: lqmao@bnu.edu.cn*

[b] *College of Chemistry, Beijing Normal University, Xinjiekouwai Street 19, Beijing 100875, China*

[c] *University of Chinese Academy of Sciences, Beijing 100049, China*

[d] *Key Laboratory of Functional Molecular Solids, Ministry of Education, College of Chemistry and Materials Science, Anhui Normal University, Wuhu 241002, China*

[e] *MOE Key Laboratory of Functional Small Organic Molecule, College of Chemistry and Chemical Engineering, Jiangxi Normal University, Nanchang 330022, China*

† Electronic supplementary information (ESI) available. See **https://doi.org/10.1039/d2sc01110g**

‡ These authors contributed equally to this work.

selective catalysts for $^1O_2$ production. However, despite some investigations on the capacity of MN_x SACs toward oxygen activation with non-selective ROS production, the atomic engineering of MN_x SACs is still needed to optimize the metal–O_2 interaction to achieve selective $^1O_2$ generation.

Here, we demonstrate a new approach to highly selective generation of $^1O_2$ from O_2 without photosensitization with single transition metal atoms anchored on hollow N-doped carbon as atomically dispersed catalysts (M_1/HNC SACs, M = Fe, Co, Cu, Ni). The $^1O_2$ generation efficiency is highly related to the metal centers, following the sequence of Fe_1/HNC > Co_1/HNC > Cu_1/HNC > Ni_1/HNC. Among the catalysts examined, the Fe_1/HNC SAC with a single atomic motif of FeN_4 coordination shows the best kinetic value of 0.140 min^{-1}, exceeding those of Co_1/HNC (0.033 min^{-1}), Cu_1/HNC (0.019 min^{-1}) and Ni_1/HNC (0.016 min^{-1}), and the single-site kinetic value of the Fe_1/HNC SAC reaches up to as high as 3.30×10^{10} min^{-1} mol^{-1}, representing top-level catalytic activity among known catalysts. Density functional theory (DFT) calculations demonstrate that the selective $^1O_2$ generation capacity originates from significant charge transfer from MN_4 sites to chemisorbed O_2, leading to the spin-flip process and spin reduction of O_2 with the lowest value of 0.25 for O_2 adsorbed on the FeN_4 site. Based on the efficient production of $^1O_2$ enabled by the Fe_1/HNC SAC, we develop a non-radiative therapeutic platform for *in vivo* inhibition of tumor cell proliferation.

Results and discussion

To synthesize M_1/HNC SACs, metal acetylacetonate encapsulated zeolitic imidazolate framework-8 (M/ZIF-8) was first synthesized as the raw material to form core–shell composites by tannic acid (TA) coating. The core–shell precursors were then pyrolyzed at 900 °C under an Ar atmosphere to obtain M_1/HNC catalysts (Fig. 1a). Hollow N-doped carbon (HNC) was prepared with pure ZIF-8 without the encapsulation of metal acetylacetonate as the control catalyst. X-ray diffraction (XRD) patterns of the catalysts show peaks for (002) and (101) planes of graphitic carbon, located at around 24° and 43°, respectively, and no observable peaks for metal-related nanoparticles were found (Fig. S1†), indicating the absence of metal nanoparticles in M_1/HNC catalysts.[39] Raman spectra of the M_1/HNC SACs and HNC reveal similar intensity ratios of the D band to the G band (Fig. S2†), suggesting that the catalysts possess a similar structure of the defective carbon skeleton. In addition, the nitrogen sorption isotherm analysis of M_1/HNC SACs and HNC (Fig. S3†)

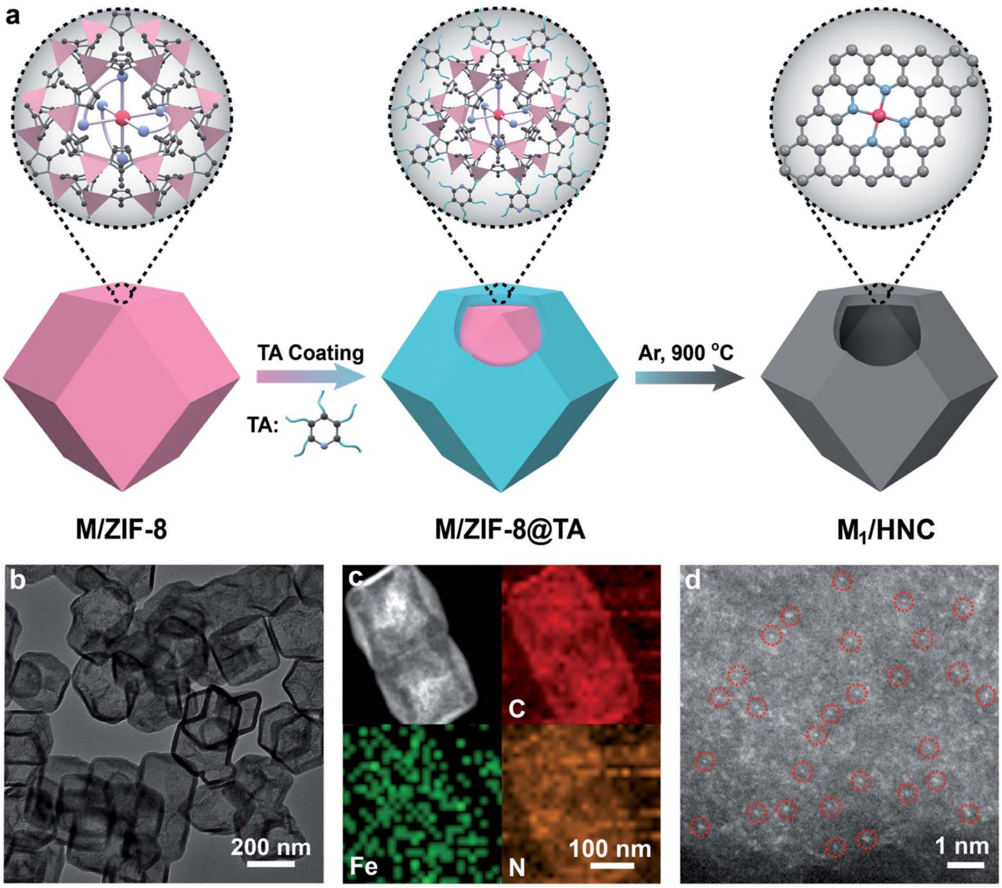

Fig. 1 Synthesis of M_1/HNC SACs and structural characterization of the Fe_1/HNC SAC. (a) Schematic depiction of the route to the fabrication of M_1/HNC SACs. (b) TEM image of Fe_1/HNC. (c) HAADF-STEM image and the corresponding elemental mapping images of Fe_1/HNC (C, red; Fe, green; N, orange). (d) Aberration-corrected HAADF-STEM image of Fe_1/HNC showing atomically dispersed Fe atoms as bright dots highlighted with red circles.

gave a similar Brunner–Emmet–Teller (BET) surface area at around 700 $cm^2\ g^{-1}$, further indicating the structural similarity of the prepared catalysts. Transmission electron microscopy (TEM) and high-angle annular dark-field scanning TEM (HAADF-STEM) images show that Fe_1/HNC has a hollow polyhedral morphology with an average size of 200 nm and thickness of 10 nm and no metal nanoparticles were observed (Fig. 1b). The elemental mapping images show a homogeneous distribution of Fe, N, and C elements over the whole domain of the Fe_1/HNC SAC (Fig. 1c). Furthermore, the aberration-corrected HAADF-STEM image was obtained to confirm single atomic Fe in the Fe_1/HNC SAC. As shown in Fig. 1d, the bright dots highlighted with red circles clearly demonstrate that the atomically dispersed Fe atoms exist over N-doped carbon. Similarly, the morphology of other three M_1/HNC SACs and the atomic dispersion were confirmed by using TEM and HAADF-STEM images, all showing a hollow polyhedral structure and atomically dispersed metal atoms (Fig. S4–S6†).

The atomic electronic structure and coordination configuration of metal species in M_1/HNC SACs were explored by X-ray absorption near-edge structure (XANES) and extended X-ray absorption fine structure (EXAFS) characterization experiments. Fig. 2a shows the XANES spectra of Fe_1/HNC at the Fe *K*-edge in comparison with those of references including Fe foil and Fe_2O_3. The peak position of Fe_1/HNC is situated between those of Fe_2O_3 and Fe foil, indicating that the valence state of the Fe atom is between 0 and +3. The Fourier-transform EXAFS spectrum of Fe_1/HNC shows only one peak at about 1.5 Å, ascribed to the first coordination shell of Fe–N, and no Fe–Fe peak like that of Fe foil at around 2.2 Å was observed (Fig. 2b), suggesting the inexistence of metal-related nanoparticles or clusters in Fe_1/HNC. In order to further investigate the atomic distribution of Fe in Fe_1/HNC, wavelet transform (WT) analysis of Fe *K*-edge EXAFS was carried out. As illustrated in Fig. 2c, only one intensity maximum at approximately 4.2 $Å^{-1}$ related to Fe–N coordination was observed from the WT contour plot of Fe_1/HNC, which is different from the contour WT plots of Fe foil and Fe_2O_3 with the intensity maximum corresponding to Fe–Fe contribution, elucidating that no Fe–Fe bond is present in Fe_1/HNC, but isolated Fe atoms exist. Moreover, the coordination configuration and structural parameters of Fe atoms were obtained from EXAFS fitting curves (Fig. 2d and S7†). As listed in Table S1,† the coordination number of Fe atoms and the bond length of Fe–N are 4.2 and 2.02 Å, respectively. From the above results, the atomic structure configuration of Fe_1/HNC was constructed (Fig. 2e). The local structure of other three M_1/HNC SACs was also confirmed with XANES and EXAFS spectra (Fig. S8–S10†), all possessing similar atomic configuration with Fe_1/HNC.

In order to systematically evaluate the oxidizing capacity of M_1/HNC SACs, the oxidation of colorless 3,3′,5,5′-tetramethylbenzidine (TMB) to blue oxidized TMB (ox-TMB) with the characteristic adsorption at *ca.* 652 nm was used as the catalytic model reaction.[40–43] Considering that the pyrolysis temperature has significant effect on the coordination microenvironment of SACs,[44,45] the TMB oxidation activities of the catalysts prepared at different temperatures were explored. As shown in Fig. 3a, the catalyst obtained at 900 °C (denoted as Fe_1/HNC-900) exhibits

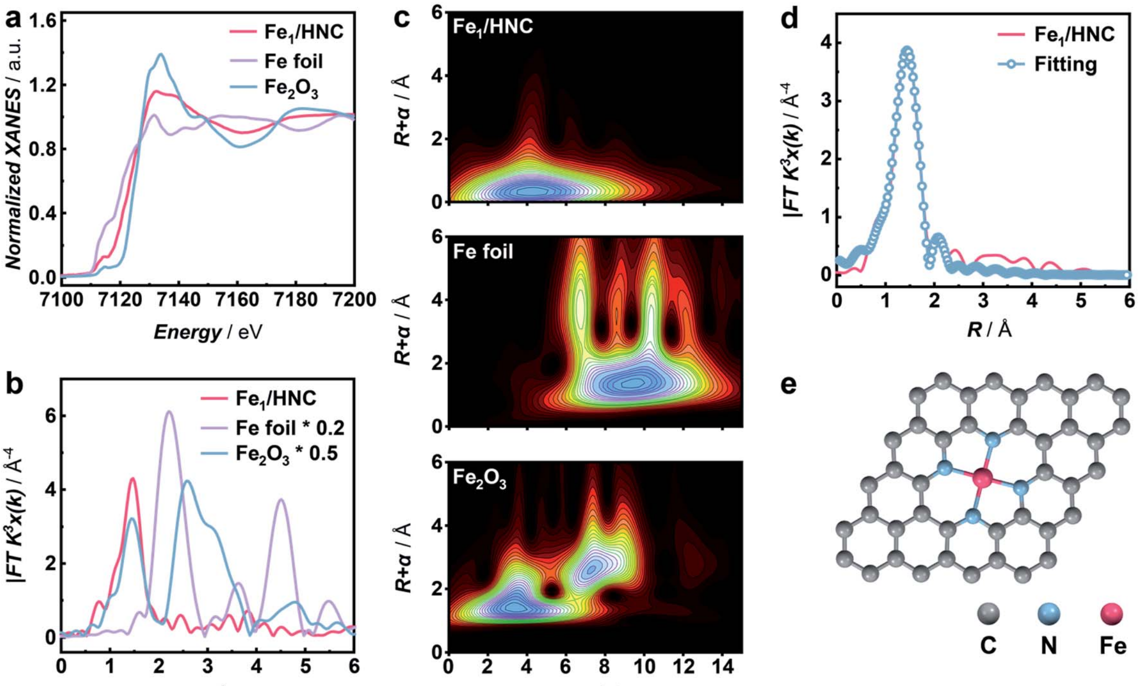

Fig. 2 XAFS analysis of the Fe_1/HNC SAC. (a) Normalized XANES spectra and (b) corresponding Fourier-transform EXAFS spectra at the Fe *K*-edge of Fe_1/HNC (red line), Fe foil (purple line), and Fe_2O_3 (blue line). (c) Wavelet transforms of the Fe *K*-edge EXAFS spectra for Fe_1/HNC, Fe foil, and Fe_2O_3. (d) Fourier-transform EXAFS spectrum and the corresponding fitting curve of Fe_1/HNC in *R*-space. (e) Schematic structure of Fe_1/HNC.

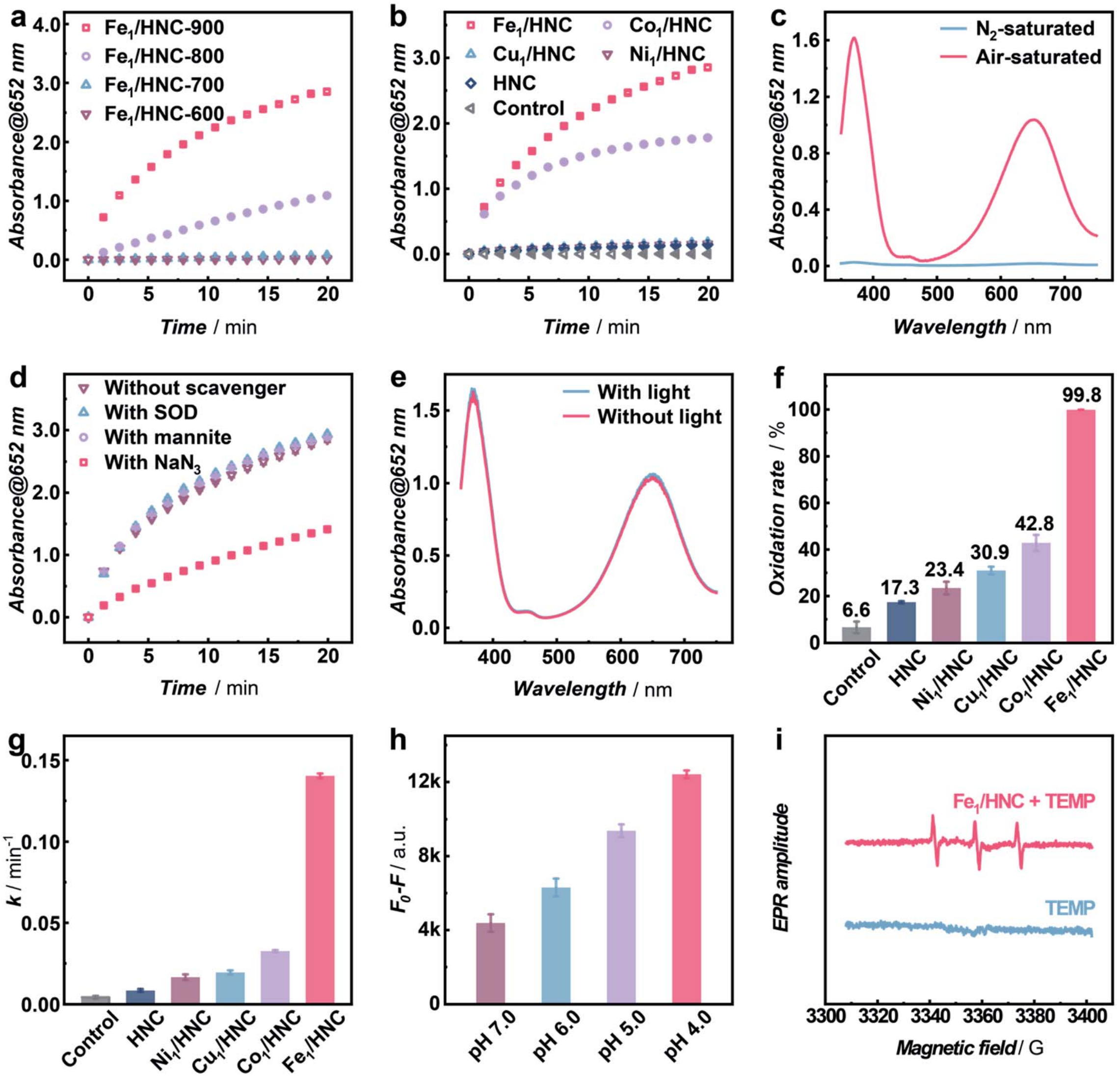

Fig. 3 Selective generation of $^1O_2$ with M_1/HNC SACs. Time-dependent absorbance changes of ox-TMB monitored at 652 nm (a) with 5 μg mL^{-1} catalysts synthesized at different temperatures or (b) with 5 μg mL^{-1} M_1/HNC and HNC in the Britton–Robinson (B–R) buffer (pH 4.0). (c) UV-vis absorption spectra of ox-TMB catalyzed by 5 μg mL^{-1} Fe_1/HNC at 2 min in the N_2-saturated (blue line) and air-saturated (red line) B–R buffer (pH 4.0). (d) Time-dependent absorbance changes of ox-TMB monitored at 652 nm catalyzed by 5 μg mL^{-1} Fe_1/HNC in the B–R buffer (pH 4.0) without scavengers (brown line) or with SOD (blue line), mannite (purple line), and NaN_3 (red line). (e) UV-vis absorption spectra of ox-TMB catalyzed by 5 μg mL^{-1} Fe_1/HNC in 2 min without (red line) or with (blue line) light in the B–R buffer (pH 4.0). (f) Oxidation rate of ABDA with M_1/HNC and HNC in the B–R buffer (pH 4.0). (g) k value of the ABDA oxidation reaction with 5 μg mL^{-1} M_1/HNC and HNC in the B–R buffer (pH 4.0). (h) Decrease in fluorescence intensity ($\lambda_{ex}/\lambda_{em} = 380/433$ nm) of ABDA with 5 μg mL^{-1} Fe_1/HNC in 5 min in the B–R buffer at different pH values. (i) TEMPO ESR signals in the absence (blue line) and presence of 20 μg mL^{-1} Fe_1/HNC in the B–R buffer (pH 4.0).

the highest catalytic activity towards TMB oxidation, and 900 °C was thus chosen to prepare other SACs. We next compared the catalytic activity of M_1/HNC SACs with different transition metal centers toward TMB oxidation. The results displayed in Fig. 3b and S11† show that the activity trends follow the sequence of Fe_1/HNC > Co_1/HNC > Cu_1/HNC > Ni_1/HNC > HNC, indicating that the single metal atom center plays a vital role in the oxidation reaction. Among the catalysts investigated, Cu_1/HNC and Ni_1/HNC SACs exhibit quite low catalytic activity towards TMB oxidation like HNC. Comparatively, both Fe_1/HNC and Co_1/HNC SACs show a high catalytic oxidation rate, far surpassing those of Cu_1/HNC and Ni_1/HNC SACs. The significant difference in catalytic performance of M_1/HNC SACs may arise from the binding strength of different MN_4 centers with O species.[46–48]

To verify whether O_2 is the only substrate for the oxidation reaction, Fe_1/HNC was selected as the representative catalyst to evaluate the TMB oxidation reaction under a N_2 atmosphere. As shown in Fig. 3c, the absorbance intensity of ox-TMB undergoes a sharp decrease in the N_2-saturated B–R buffer compared with that under air-saturated conditions, indicating the indispensable role of O_2 in the oxidation of TMB catalyzed by the Fe_1/HNC SAC. In addition, as displayed in Fig. S12–S15,† the catalytic

TMB oxidation reaction with M_1/HNC (Fe_1/HNC and Co_1/HNC as examples) is dose- and pH-dependent.

It is generally known that the catalytic oxidation reactions with O_2 are always accompanied with the generation of ROS like $^{\bullet}OH$, O_2^- and $^1O_2$, thus, it is vital to identify the exact species produced during the process of the oxidation reaction by M_1/HNC SACs. For this purpose, mannite, superoxide dismutase (SOD), and NaN_3 were chosen as the ROS scavengers for $^{\bullet}OH$, O_2^-, and $^1O_2$, respectively.[49] Notably, only NaN_3 exhibits efficient inhibitation of TMB oxidation catalyzed by the Fe_1/HNC SAC, while the others display no obvious effects on the oxidation reaction (Fig. 3d), suggesting that the Fe_1/HNC SAC selectively activates O_2 into $^1O_2$. In consideration of photosensitization usually implemented to produce $^1O_2$, the comparison of the Fe_1/HNC-catalyzed TMB oxidation reaction under normal light conditions and in a dark environment was performed. As shown in Fig. 3e, a negligible difference in characteristic absorbance of ox-TMB was observed, indicating the striking generation of $^1O_2$ without photosensitization. Collectively, highly selective generation of $^1O_2$ from O_2 can be achieved by using the Fe_1/HNC SAC without the assistance of the externally applied stimulus.

To further validate the selective production of $^1O_2$ from O_2 enabled by M_1/HNC SACs, an $^1O_2$-specific probe 9,10-anthracenediyl-bis(methylene) dimalonic acid (ABDA) was adopted to selectively recognize and react with $^1O_2$.[50,51] ABDA is a fluorescent molecule with λ_{ex} and λ_{em} at *ca.* 380 nm and 433 nm, respectively, which turns to be a non-fluorescent endoperoxide product upon selective oxidation by $^1O_2$ *via* a [4 + 2]-cycloaddition. With ABDA as the probe, we evaluated the catalytic efficiency of M_1/HNC SACs in generating $^1O_2$ from O_2. As can be seen in Fig. 3f and S16,† the activity towards ABDA oxidation follows the rate sequence of Fe_1/HNC (99.8%) > Co_1/HNC (42.8%) > Cu_1/HNC (30.9%) > Ni_1/HNC (23.4%) > HNC (17.3%), which is consistent with the trends in TMB oxidation. Notably, Fe_1/HNC displays the highest catalytic activity toward

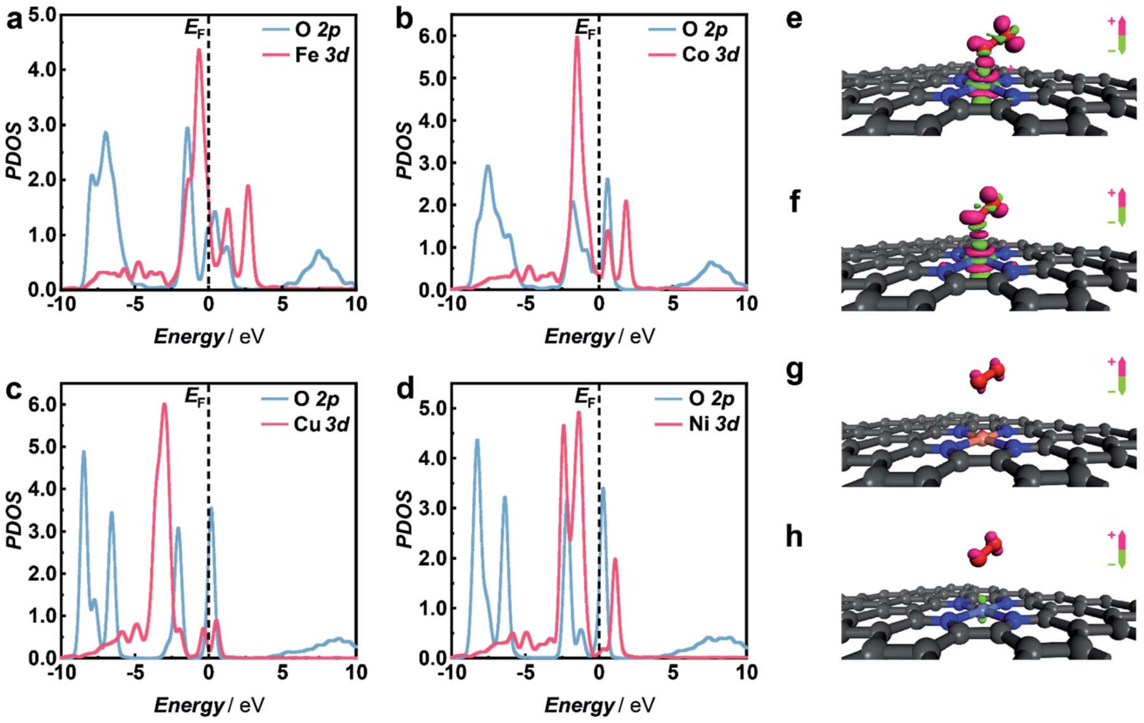

i

MN_4	O_2 Ads. Energy (eV)	O-O Bond Length (ads)	Bader Charge of O_2 (ads)	Hirshfeld Spin of M	Hirshfeld Spin of M (ads)	Hirshfeld Spin of O	Hirshfeld Spin of O (ads)
FeN_4	-1.039	1.284	-0.44	1.89	0.31	1	0.25
CoN_4	-0.848	1.269	-0.43	0.41	0.03	1	0.46
CuN_4	-0.272	1.235	-0.21	0.53	0.51	1	0.91
NiN_4	-0.244	1.233	-0.18	0	0.11	1	0.92

Fig. 4 DFT calculations. PDOS of the M 3d (red line) and O 2p (blue line) orbitals of (a) FeN_4, (b) CoN_4, (c) CuN_4 and (d) NiN_4 sites adsorbed with O_2. Calculated charge density differences of (e) FeN_4, (f) CoN_4, (g) CuN_4 and (h) NiN_4 centers adsorbed with O_2. (i) Comparison of the DFT results for constructed MN_4 structures.

ABDA oxidation with a rate of nearly 100%, indicative of more efficient $^1O_2$ generation catalyzed by Fe_1/HNC in comparison with other SACs. In addition, the kinetic profiles of ABDA oxidation were examined to assess $^1O_2$ generation capacities of M_1/HNC SACs by calculating the oxidation rate of ABDA with pseudo-first-order approximation. As shown in Fig. S17,† an exponential decrease in the fluorescence intensity of ABDA against the reaction time was observed and the pseudo-first-order kinetic constants (*k* values) were obtained from the linear relationship. The results shown in Fig. 3g reveal that Fe_1/HNC catalyzes the generation of $^1O_2$ for ABDA oxidation with a *k* value of 0.140 min^{-1}, considerably higher than that of Co_1/HNC (0.033 min^{-1}), Cu_1/HNC (0.019 min^{-1}) and Ni_1/HNC (0.016 min^{-1}), further highlighting the critical role of different single metal atom coordination. The single-site kinetic constant ($k_{\text{single-site}}$ value) of the Fe_1/HNC SAC was further evaluated to be as high as 3.30×10^{10} min^{-1} mol^{-1} due to the high catalytic efficiency with a low metal content of 0.17 wt% determined *via* inductively coupled plasma optical emission spectrometry (ICP-OES). Besides, the Fe_1/HNC-enabled selective generation of $^1O_2$ was investigated with different concentrations of the catalyst and in reaction media with different pH values (Fig. 3h and S18†). As shown in Fig. S19,† the ABDA oxidation reaction shows a dose-dependent behavior. In addition, the generation of $^1O_2$ for ABDA oxidation is peculiarly prone to occur under acidic conditions.

To further confirm the selective generation of $^1O_2$ enabled by Fe_1/HNC, colorimetric and fluorescent probes for other ROSs were utilized, thereinto, ρ-phthalic acid (PTA) and iodonitrotetrazolium chloride (INT) were selected to detect $^{\bullet}OH$, and O_2^-, respectively. PTA, as a widely used $^{\bullet}OH$ probe, can be selectively hydroxylated upon reaction with $^{\bullet}OH$ to form 2-hydroxy terephthalic acid with strong fluorescence at $\lambda_{ex}/\lambda_{em} = 315/400$ nm.[52] INT is a specific probe for O_2^-, which can be reduced by O_2^- to generate the colored formanzan product with the maximum absorption at 510 nm. As shown in Fig. S20,† no obvious changes in the fluorescence intensity of PTA or absorbance of INT were observed in the oxidation reaction, demonstrating negligible generation of $^{\bullet}OH$ and O_2^- but highly selective production of $^1O_2$ during the O_2 activation process. Furthermore, electron spin resonance (ESR) characterization using 2,2,6,6-tetramethylpiperidine (TEMP) as the $^1O_2$ trapping agent and 5-*tert*-butoxycarbonyl-5-methyl-1-pyrroline *N*-oxide (BMPO) as the trapping agent for $^{\bullet}OH$ and O_2^- were also conducted to give more direct evidence of the produced ROS.[53,54] Fig. 3i shows the typical 1 : 1 : 1 triplet ESR signal for 2,2,6,6-tetramethylpiperidine-*N*-oxyl (TEMPO) formed due to the $^1O_2$ generation in the presence of the Fe_1/HNC SAC. However, there are no observable signals when BMPO was used as the trapping agent (Fig. S21†), indicating that negligible $^{\bullet}OH$ and O_2^- are produced in the process of Fe_1/HNC-catalyzed O_2 activation.

To gain in-depth insight into the mechanism of selective $^1O_2$ generation enabled by M_1/HNC SACs, DFT calculations were performed to explore the electronic structure of the active sites and their interactions with O_2.[55–58] In accordance with the atomic structural analysis, the models of M_1/HNC SACs adsorbed with O_2 were constructed and optimized. The adsorption energy of O_2 on the FeN_4 site in the Fe_1/HNC SAC was calculated to be −1.039 eV, which is less than those of other M_1/HNC SACs (Fig. 4i), illustrating the strong interaction between the FeN_4 site and O_2. In order to further elucidate the electronic interactions between MN_4 sites and absorbed O_2, the projected density of states (PDOS) for M 3d and O 2p was calculated. As shown in Fig. 4a–d, more hybridization between the PDOS for Fe 3d orbitals and O 2p orbitals can be evidently observed in contrast with those for CuN_4 or NiN_4 centers. Meanwhile, the Fe 3d orbitals shift toward the Fermi level upon O_2 adsorption (Fig. S22–S25†), further demonstrating the occurrence of O_2 activation on FeN_4.[59,60] In addition, the Bader charge analysis and charge density difference analysis (Fig. 4e–h) reveal distinct charge transfer with 0.44 e from the FeN_4 site to O_2, leading to the elongation of the O–O bond with a length from 1.22 Å in free O_2 to 1.284 Å in O_2 adsorbed on the FeN_4 site (Fig. 4i), which is longer than those on other MN_4 sites. The longest O–O bond of O_2 upon adsorption on the FeN_4 site manifests the strongest interaction between the FeN_4 site and O_2. The transferred electrons will occupy the half-filled antibonding π* orbitals of O_2 and give rise to the reduction of the Hirshfeld spin value of O_2 from 1 in free O_2 to 0.25, suggesting that a significant spin-flip process occurs for chemisorbed O_2 on the FeN_4 site. The spin value of O_2 upon chemisorption on the FeN_4 site (0.25) is close to that of $^1O_2$ (0) and relatively lower than those on other MN_4 sites, elucidating the superior capacity of the FeN_4 site toward the generation of $^1O_2$. Given the above, the charge transfer from the MN_4 site to adsorbed O_2 contributes to different spin-flip degrees of O_2, thus bringing about a discrepancy in their capacities toward selective $^1O_2$ generation.

Having demonstrated the high efficiency of selective $^1O_2$ generation without photosensitization from molecular O_2 enabled by the Fe_1/HNC SAC, we then employed the Fe_1/HNC SAC as a therapeutic agent for suppressing tumor cell growth. To improve the dispersibility and biocompatibility of Fe_1/HNC, an amphipathic molecule DSPE-PEG2000 was modified on the surface of Fe_1/HNC to form PEGylated Fe_1/HNC (donated as P-Fe_1/HNC) through the hydrophobic interaction.[61] The cellular uptake of P-Fe_1/HNC was visualized by confocal laser scanning microscopy (CLSM) imaging with fluorescein isothiocyanate (FITC)-loaded P-Fe_1/HNC. As displayed in Fig. 5a and S26,† the bright green fluorescence and the black dots in cytosol clearly indicate the efficient internalization of P-Fe_1/HNC in HeLa cells. Next, the inhibition effect of P-Fe_1/HNC on cell proliferation was systematically explored by the cell viability test with a standard MTT [3-(4,5-dimethylthiazol-2-yl)-2,5-diphenyltetrazolium] assay. The results show that the treatment of HeLa cells with PEGylated HNC (P-HNC) without single Fe atomic centers exhibits a negligible effect on the proliferation of HeLa cells with cell viability exceeding 90% even at a concentration of P-HNC as high as 0.3 mg mL^{-1} (Fig. 5b), indicating the excellent biocompatibility and low cytotoxicity of P-HNC. In striking contrast, an obvious decrease in cell viability of HeLa cells to less than 50% upon the treatment of P-Fe_1/HNC with a low concentration of 0.06 mg mL^{-1} was observed and the cell viability decreases with increasing P-Fe_1/HNC concentration,

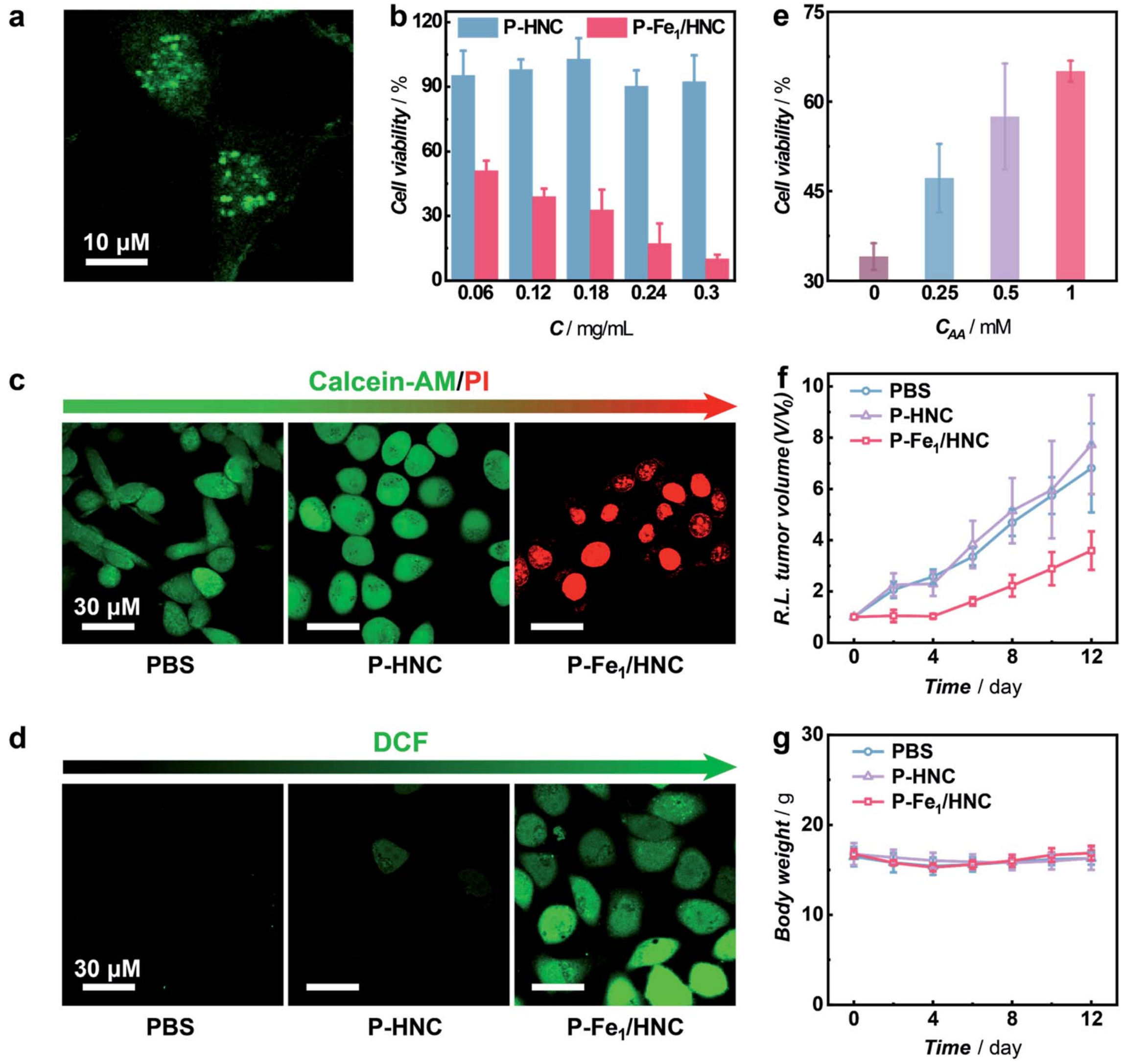

Fig. 5 *In vitro* and *in vivo* inhibition of tumor growth with the Fe$_1$/HNC SAC. (a) CLSM fluorescence image of HeLa cells treated with FITC-loaded P-Fe$_1$/HNC for 6 h. (b) Cell viability of HeLa cells after 12 h-treatment of P-HNC or P-Fe/HNC at the concentrations of 0.06–0.3 mg mL^{-1}. CLSM fluorescence images of HeLa cells stained with Calcein-AM and (c) PI or (d) DCFH-DA after the 12 h-treatment with PBS, P-HNC and P-Fe$_1$/HNC. (e) Cell viability of HeLa cells pre-incubated with AA (0.25 mM, 0.5 mM, and 1 mM) after 12 h-treatment with 0.1 mg mL^{-1} P-Fe/HNC. *In vivo* (f) tumor proliferation and (g) body weight curves of mice treated with the intravenous injection of PBS (blue line), P-HNC (purple line), or P-Fe$_1$/HNC (red line).

providing direct evidence for the antiproliferation effect on HeLa cells.

In the meantime, the cytotoxicity of P-Fe$_1$/HNC was further investigated by co-staining HeLa cells with calcein-AM (green fluorescent dye for viable cell staining) and propidium iodide (PI, red fluorescent dye for dead cell staining) and visualized with CLSM imaging.[62] As exhibited in Fig. 5c and S27,† in comparison with the group treated with PBS or P-HNC showing bright green fluorescence, cancer cells treated with P-Fe$_1$/HNC show strong red fluorescence, indicating the high cytotoxicity against HeLa cells of Fe$_1$/HNC SACs. According to the results demonstrated above, such capacity of killing cancer cells was deemed to originate from the intracellular oxidative stress induced by Fe$_1$/HNC SAC-enabled selective production of $^1O_2$, which was distinctly confirmed with a cell-permeable ROS-sensitive probe (2′,7′-dichlorofluorescein diacetate, DCFH-DA).[63,64] Obviously, cancer cells treated with P-Fe$_1$/HNC show the brightest green fluorescence of DCF (Fig. 5d and S28†), indicative of most $^1O_2$ generation enabled by Fe$_1$/HNC. In order to further demonstrate the cytotoxicity against HeLa cells of the Fe$_1$/HNC SAC from the oxidative damage induced by the generation of $^1O_2$, ascorbic acid (AA) as an antioxidant was used to pre-incubate HeLa cells.[61] As shown in Fig. 5e, the pre-incubation of AA can efficiently reduce the cytotoxicity of the Fe$_1$/HNC SAC through the elimination of generated $^1O_2$ with a concentration-dependent behavior.

The antitumor effect of the Fe$_1$/HNC SAC *in vivo* was also investigated with HeLa tumor-bearing mice as a model. When the tumor volume reached about 100 mm^3, the mice were randomly divided into three groups and intravenously injected with PBS, P-HNC, and P-Fe_1/HNC, respectively. As shown in Fig. 5f, the mice treated with P-HNC exhibit a similar tumor growth tendency with that of PBS, indicating that HNC had no obvious therapeutic effect on suppressing tumor growth. In contrast, the group treated with P-Fe_1/HNC displays a relatively higher tumor inhibition effect with the reduction of the tumor size to 46.5% in 12 days compared with the control group, which was attributed to the high capacity of the Fe_1/HNC SAC for $^1O_2$ generation within the tumor site. Moreover, photographs of the excised tumors further confirmed the good anti-tumor effect of Fe_1/HNC (Fig. S29†). In addition, no obvious changes of the body weight of mice were observed during the experimental period upon administration of different catalysts, indicating the favorable biocompatibility of the Fe_1/HNC SAC (Fig. 5g). Further blood biochemical analysis also implied the good biosafety of these catalysts (Fig. S30†).

Conclusions

In summary, we have demonstrated that atomically dispersed MN_4 sites on hollow N-doped carbon can be used for the selective generation of strong oxidizing $^1O_2$ from O_2 without photosensitization. The as-prepared M_1/HNC SACs show different $^1O_2$ generation efficiencies in the sequence of Fe_1/HNC > Co_1/HNC > Cu_1/HNC > Ni_1/HNC. Among the developed catalysts, the Fe_1/HNC SAC shows the best kinetic value of 0.14 min^{-1} and a single-site kinetic value of 3.30×10^{10} min^{-1} mol^{-1}, originating from the spin-flip process and spin reduction of O_2 to 0.25 induced *via* significant charge transfer with 0.44 e from the FeN_4 site to O_2. More importantly, the Fe_1/HNC SAC with superior $^1O_2$ generation capacity has been successfully utilized as an efficient non-radiative therapeutic agent for inhibiting tumor cell proliferation *in vitro* and *in vivo*. We believe that this finding would provide a facile method for the selective production of $^1O_2$, opening up a new avenue for the development of functional SACs in biomedical applications.

Data availability

All experimental and computational data is available in the ESI.†

Author contributions

L. M., W. M. and J. M. conceived the idea for the project. W. M. and J. M. designed the experiments and conducted material synthesis, structural characterization, performance test and data analysis. C. H. carried out the DFT calculations. L. S. contributed to the animal experiments. J. L. and M. W. helped in the cell experiments. P. Y. contributed to the discussion of the catalytic part. W. M. drafted the manuscript, and L. M. finalized the manuscript. All authors discussed and commented on the manuscript.

Conflicts of interest

There are no conflicts to declare.

Acknowledgements

We acknowledge financial support from the National Key Research and Development Program (2018YFE0200800), the National Natural Science Foundation of China (Grant No. 22134002, 21790390 and 21790391 for L. M., 21705155 and 21790392 for W. M., 21971002 for J. M., and 21775151 and 21790053 for P. Y.), the National Basic Research Program of China (2016YFA0200104 and 2018YFA0703501), and the Strategic Priority Research Program of Chinese Academy of Sciences (XDB30000000). Beijing Academy of Science and Technology (BJAST) Scholar Programs (B), and Beijing Municipal Financial Project (PXM2021_178305_000004). All the animal experiments were conducted with the guidelines of the Animal Advisory Committee at the State Key Laboratory of Cognitive Neuroscience and Learning, and were approved by the Institutional Animal Care and Use Committee at Beijing Normal University.

Notes and references

1 Z. Li, Z. Wang, N. Chekshin, S. Qian, J. X. Qiao, P. T. Cheng, K.-S. Yeung, W. R. Ewing and J.-Q. Yu, *Science*, 2021, **372**, 1452–1457.
2 R. A. Copeland, S. Zhou, I. Schaperdoth, T. K. C. Shoda, J. M. Bollinger and C. Krebs, *Science*, 2021, **373**, 1489–1493.
3 T. Richards, J. H. Harrhy, R. J. Lewis, A. G. R. Howe, G. M. Suldecki, A. Folli, D. J. Morgan, T. E. Davies, E. J. Loveridge, D. A. Crole, J. K. Edwards, P. Gaskin, C. J. Kiely, Q. He, D. M. Murphy, J.-Y. Maillard, S. J. Freakley and G. J. Hutchings, *Nat. Catal.*, 2021, **4**, 575–585.
4 Y. Wang, S. Liu, C. Pei, Q. Fu, Z.-J. Zhao, R. Mu and J. Gong, *Chem. Sci.*, 2019, **10**, 10531–10536.
5 M. Ansari, D. Senthilnathan and G. Rajaraman, *Chem. Sci.*, 2020, **11**, 10669–10687.
6 B. Qiao, A. Wang, X. Yang, L. F. Allard, Z. Jiang, Y. Cui, J. Liu, J. Li and T. Zhang, *Nat. Chem.*, 2011, **3**, 634–641.
7 A. Jose, A. W. Schaefer, A. C. Roveda, W. J. Transue, S. K. Choi, Z. Ding, R. B. Gennis and E. I. Solomon, *Science*, 2021, **373**, 1225–1229.
8 W. Peng, X. Qu, S. Shaik and B. Wang, *Nat. Catal.*, 2021, **4**, 266–273.
9 M. Wikström, K. Krab and V. Sharma, *Chem. Rev.*, 2018, **118**, 2469–2490.
10 A. McEvoy, J. Creutzberg, R. K. Singh, M. J. Bjerrum and E. D. Hedegård, *Chem. Sci.*, 2021, **12**, 352–362.
11 B. Yang, Y. Chen and J. Shi, *Chem. Rev.*, 2019, **119**, 4881–4985.
12 C. P. Stanley, G. J. Maghzal, A. Ayer, J. Talib, A. M. Giltrap, S. Shengule, K. Wolhuter, Y. Wang, P. Chadha, C. Suarna, O. Prysyazhna, J. Scotcher, L. L. Dunn, F. M. Prado, N. Nguyen, J. O. Odiba, J. B. Baell, J.-P. Stasch, Y. Yamamoto, P. Di Mascio, P. Eaton, R. J. Payne and R. Stocker, *Nature*, 2019, **566**, 548–552.
13 M. Agrachev, W. Fei, S. Antonello, S. Bonacchi, T. Dainese, A. Zoleo, M. Ruzzi and F. Maran, *Chem. Sci.*, 2020, **11**, 3427–3440.

14 H.-B. Cheng, B. Qiao, H. Li, J. Cao, Y. Luo, K. M. Kotraiah Swamy, J. Zhao, Z. Wang, J. Y. Lee, X.-J. Liang and J. Yoon, *J. Am. Chem. Soc.*, 2021, **143**, 2413–2422.

15 P. Di Mascio, G. R. Martinez, S. Miyamoto, G. E. Ronsein, M. H. G. Medeiros and J. Cadet, *Chem. Rev.*, 2019, **119**, 2043–2086.

16 H. Zhang, D. Yu, S. Liu, C. Liu, Z. Liu, J. Ren and X. Qu, *Angew. Chem., Int. Ed.*, 2022, **61**, e202109068.

17 Z. Zheng, H. Liu, S. Zhai, H. Zhang, G. Shan, R. T. K. Kwok, C. Ma, H. H. Y. Sung, I. D. Williams, J. W. Y. Lam, K. S. Wong, X. Hu and B. Z. Tang, *Chem. Sci.*, 2020, **11**, 2494–2503.

18 M. Huo, L. Wang, L. Zhang, C. Wei, Y. Chen and J. Shi, *Angew. Chem., Int. Ed.*, 2020, **59**, 1906–1913.

19 C. Wu, Z. Liu, Z. Chen, D. Xu, L. Chen, H. Lin and J. Shi, *Sci. Adv.*, 2021, **7**, eabj8833.

20 F. Gao, T. Shao, Y. Yu, Y. Xiong and L. Yang, *Nat. Commun.*, 2021, **12**, 745.

21 Y. Zhao, M. Sun, X. Wang, C. Wang, D. Lu, W. Ma, S. A. Kube, J. Ma and M. Elimelech, *Nat. Commun.*, 2020, **11**, 6228.

22 Y. Gao, T. Wu, C. Yang, C. Ma, Z. Zhao, Z. Wu, S. Cao, W. Geng, Y. Wang, Y. Yao, Y. Zhang and C. Cheng, *Angew. Chem., Int. Ed.*, 2021, **60**, 22513–22521.

23 H. Ma, S. Long, J. Cao, F. Xu, P. Zhou, G. Zeng, X. Zhou, C. Shi, W. Sun, J. Du, K. Han, J. Fan and X. Peng, *Chem. Sci.*, 2021, **12**, 13809–13816.

24 X. Mi, P. Wang, S. Xu, L. Su, H. Zhong, H. Wang, Y. Li and S. Zhan, *Angew. Chem., Int. Ed.*, 2021, **60**, 4588–4593.

25 Z. Yang, J. Qian, A. Yu and B. Pan, *Proc. Natl. Acad. Sci. U.S.A.*, 2019, **116**, 6659–6664.

26 L.-S. Zhang, X.-H. Jiang, Z.-A. Zhong, L. Tian, Q. Sun, Y.-T. Cui, X. Lu, J.-P. Zou and S.-L. Luo, *Angew. Chem., Int. Ed.*, 2021, **60**, 21751–21755.

27 B. F. Sels, D. E. De Vos and P. A. Jacobs, *J. Am. Chem. Soc.*, 2007, **129**, 6916–6926.

28 T. Chen, P. Hou, Y. Zhang, R. Ao, L. Su, Y. Jiang, Y. Zhang, H. Cai, J. Wang, Q. Chen, J. Song, L. Lin, H. Yang and X. Chen, *Angew. Chem., Int. Ed.*, 2021, **60**, 15006–15012.

29 X. Ye, Y. Li, P. Luo, B. He, X. Cao and T. Lu, *Nano Res.*, 2021, **15**, 1509–1516.

30 T. Luo, G. T. Nash, Z. Xu, X. Jiang, J. Liu and W. Lin, *J. Am. Chem. Soc.*, 2021, **143**, 13519–13524.

31 D. Mao, F. Hu, Z. Yi, Kenry, S. Xu, S. Yan, Z. Luo, W. Wu, Z. Wang, D. Kong, X. Liu and B. Liu, *Sci. Adv.*, 2020, **6**, eabb2712.

32 Z. Li, S. Ji, Y. Liu, X. Cao, S. Tian, Y. Chen, Z. Niu and Y. Li, *Chem. Rev.*, 2020, **120**, 623–682.

33 R. Lang, X. Du, Y. Huang, X. Jiang, Q. Zhang, Y. Guo, K. Liu, B. Qiao, A. Wang and T. Zhang, *Chem. Rev.*, 2020, **120**, 11986–12043.

34 H. Jing, P. Zhu, X. Zheng, Z. Zhang, D. Wang and Y. Li, *Adv. Powder Mater.*, 2022, **1**, 100013.

35 X. Zhang, H. Lin, J. Zhang, Y. Qiu, Z. Zhan, Q. Xu, G. Meng, W. Yan, L. Gu, L. Zheng, D. Wang and Y. Li, *Chem. Sci.*, 2021, **12**, 14599–14605.

36 Y. Xiong, W. Sun, Y. Han, P. Xin, X. Zheng, W. Yan, J. Dong, J. Zhang, D. Wang and Y. Li, *Nano Res.*, 2021, **14**, 2418–2423.

37 X.-P. Qin, S.-Q. Zhu, L.-L. Zhang, S.-H. Sun and M.-H. Shao, *J. Electrochem.*, 2021, **27**, 185–194.

38 W. Ma, F. Wu, P. Yu and L. Mao, *Chem. Sci.*, 2021, **12**, 7908–7917.

39 Z. Li, Y. Chen, S. Ji, Y. Tang, W. Chen, A. Li, J. Zhao, Y. Xiong, Y. Wu, Y. Gong, T. Yao, W. Liu, L. Zheng, J. Dong, Y. Wang, Z. Zhuang, W. Xing, C.-T. He, C. Peng, W.-C. Cheong, Q. Li, M. Zhang, Z. Chen, N. Fu, X. Gao, W. Zhu, J. Wan, J. Zhang, L. Gu, S. Wei, P. Hu, J. Luo, J. Li, C. Chen, Q. Peng, X. Duan, Y. Huang, X.-M. Chen, D. Wang and Y. Li, *Nat. Chem.*, 2020, **12**, 764–772.

40 S. Ji, B. Jiang, H. Hao, Y. Chen, J. Dong, Y. Mao, Z. Zhang, R. Gao, W. Chen, R. Zhang, Q. Liang, H. Li, S. Liu, Y. Wang, Q. Zhang, L. Gu, D. Duan, M. Liang, D. Wang, X. Yan and Y. Li, *Nat. Catal.*, 2021, **4**, 407–417.

41 X. Chen, L. Zhao, K. Wu, H. Yang, Q. Zhou, Y. Xu, Y. Zheng, Y. Shen, S. Liu and Y. Zhang, *Chem. Sci.*, 2021, **12**, 8865–8871.

42 B. Xu, H. Wang, W. Wang, L. Gao, S. Li, X. Pan, H. Wang, H. Yang, X. Meng, Q. Wu, L. Zheng, S. Chen, X. Shi, K. Fan, X. Yan and H. Liu, *Angew. Chem., Int. Ed.*, 2019, **58**, 4911–4916.

43 L. Huang, J. Chen, L. Gan, J. Wang and S. Dong, *Sci. Adv.*, 2019, **5**, eaav5490.

44 S. Ji, Y. Chen, X. Wang, Z. Zhang, D. Wang and Y. Li, *Chem. Rev.*, 2020, **120**, 11900–11955.

45 X. Li, H. Rong, J. Zhang, D. Wang and Y. Li, *Nano Res.*, 2020, **13**, 1842–1855.

46 F. Luo, A. Roy, L. Silvioli, D. A. Cullen, A. Zitolo, M. T. Sougrati, I. C. Oguz, T. Mineva, D. Teschner, S. Wagner, J. Wen, F. Dionigi, U. I. Kramm, J. Rossmeisl, F. Jaouen and P. Strasser, *Nat. Mater.*, 2020, **19**, 1215–1223.

47 C.-X. Zhao, B.-Q. Li, J.-N. Liu and Q. Zhang, *Angew. Chem., Int. Ed.*, 2021, **60**, 4448–4463.

48 C. Tang, L. Chen, H. Li, L. Li, Y. Jiao, Y. Zheng, H. Xu, K. Davey and S.-Z. Qiao, *J. Am. Chem. Soc.*, 2021, **143**, 7819–7827.

49 H. Wang, S. Jiang, S. Chen, D. Li, X. Zhang, W. Shao, X. Sun, J. Xie, Z. Zhao, Q. Zhang, Y. Tian and Y. Xie, *Adv. Mater.*, 2016, **28**, 6940–6945.

50 M. Wang, Y. Zhang, M. Ng, A. Skripka, T. Cheng, X. Li, K. K. Bhakoo, A. Y. Chang, F. Rosei and F. Vetrone, *Chem. Sci.*, 2020, **11**, 6653–6661.

51 H. Chen, S. Li, M. Wu, Kenry, Z. Huang, C.-S. Lee and B. Liu, *Angew. Chem., Int. Ed.*, 2020, **59**, 632–636.

52 F. Cao, L. Zhang, Y. You, L. Zheng, J. Ren and X. Qu, *Angew. Chem., Int. Ed.*, 2020, **59**, 5108–5115.

53 Q. Liu, K. Wan, Y. Shang, Z.-G. Wang, Y. Zhang, L. Dai, C. Wang, H. Wang, X. Shi, D. Liu and B. Ding, *Nat. Mater.*, 2021, **20**, 395–402.

54 X. Hu, F. Li, F. Xia, X. Guo, N. Wang, L. Liang, B. Yang, K. Fan, X. Yan and D. Ling, *J. Am. Chem. Soc.*, 2020, **142**, 1636–1644.

55 H.-Y. Zhuo, X. Zhang, J.-X. Liang, Q. Yu, H. Xiao and J. Li, *Chem. Rev.*, 2020, **120**, 12315–12341.

56 L. Li, X. Chang, X. Lin, Z.-J. Zhao and J. Gong, *Chem. Soc. Rev.*, 2020, **49**, 8156–8178.

57 X. Li, C.-S. Cao, S.-F. Hung, Y.-R. Lu, W. Cai, A. I. Rykov, S. Miao, S. Xi, H. Yang, Z. Hu, J. Wang, J. Zhao, E. E. Alp, W. Xu, T.-S. Chan, H. Chen, Q. Xiong, H. Xiao, Y. Huang, J. Li, T. Zhang and B. Liu, *Chem*, 2020, **6**, 3440–3454.

58 Y. Pan, Y. Chen, K. Wu, Z. Chen, S. Liu, X. Cao, W.-C. Cheong, T. Meng, J. Luo, L. Zheng, C. Liu, D. Wang, Q. Peng, J. Li and C. Chen, *Nat. Commun.*, 2019, **10**, 4290.

59 R. Gao, J. Wang, Z.-F. Huang, R. Zhang, W. Wang, L. Pan, J. Zhang, W. Zhu, X. Zhang, C. Shi, J. Lim and J.-J. Zou, *Nat. Energy*, 2021, **6**, 614–623.

60 K. Chen, K. Liu, P. An, H. Li, Y. Lin, J. Hu, C. Jia, J. Fu, H. Li, H. Liu, Z. Lin, W. Li, J. Li, Y.-R. Lu, T.-S. Chan, N. Zhang and M. Liu, *Nat. Commun.*, 2020, **11**, 4173.

61 M. Huo, L. Wang, Y. Wang, Y. Chen and J. Shi, *ACS Nano*, 2019, **13**, 2643–2653.

62 R. Xiong, D. Hua, J. Van Hoeck, D. Berdecka, L. Léger, S. De Munter, J. C. Fraire, L. Raes, A. Harizaj, F. Sauvage, G. Goetgeluk, M. Pille, J. Aalders, J. Belza, T. Van Acker, E. Bolea-Fernandez, T. Si, F. Vanhaecke, W. H. De Vos, B. Vandekerckhove, J. van Hengel, K. Raemdonck, C. Huang, S. C. De Smedt and K. Braeckmans, *Nat. Nanotechnol.*, 2021, **16**, 1281–1291.

63 T. Xiong, M. Li, Y. Chen, J. Du, J. Fan and X. Peng, *Chem. Sci.*, 2021, **12**, 2515–2520.

64 R. Cai, H. Xiang, D. Yang, K.-T. Lin, Y. Wu, R. Zhou, Z. Gu, L. Yan, Y. Zhao and W. Tan, *J. Am. Chem. Soc.*, 2021, **143**, 16113–16127.